The Astrophysical Journal, 991:162 (7pp), 2025 October 1 https://doi.org/10.3847/1538-4357/adf8e6

XMM-Newton View of Pulsating Iron Fluorescent Emission from Centaurus X-3

Kinjal Roy[1], Hemanth Manikantan[1,2], and Biswajit Paul[1]
[1] Raman Research Institute, C. V. Raman Avenue, Sadashivanagar, Bengaluru—560 080, India
[2] INAF—Istituto di Astrofisica e Planetologia Spaziali, Via del Fosso del Cavaliere, 100, 00133 Roma, Italy
Received 2025 June 9; revised 2025 July 26; accepted 2025 August 5; published 2025 September 25

Abstract

Centaurus X–3 (Cen X–3) is a bright, high-mass X-ray binary pulsar. We present a pulse phase–resolved X-ray spectral analysis of data from an archival XMM-Newton observation of Cen X–3 taken during the high state of the source. The observation was entirely in the out-of-eclipse part of the binary orbit. We study the pulse phase variability of the three Kα fluorescent emission lines from near-neutral, helium-like, and hydrogen-like iron, along with the iron Kβ emission line. All four lines show clear modulation with the pulse phase of the neutron star (NS), and modulation is found to be higher for the lines from highly ionised iron compared to the neutral lines. Structures within the light travel distance corresponding to the pulse period of the NS are likely responsible for the pulse phase modulation of the emission lines. We have also investigated the orbital phase dependence of the pulse phase variability in the iron lines by dividing the data into four segments at different orbital phases of Cen X–3. The pulse phase modulation behavior of the four lines is quite identical at different orbital phases of Cen X–3, indicating the pulsed iron emission region is persistent in nature and probably phase aligned with respect to the observer. The accretion stream intercepting the line of sight can probably produce the observed phase dependence of the iron fluorescence emission lines.

Unified Astronomy Thesaurus concepts: X-ray binary stars (1811); High mass x-ray binary stars (733); X-ray astronomy (1810); Binary pulsars (153); Neutron stars (1108)

1. Introduction

Centaurus X–3 (Cen X–3) is a high-mass X-ray binary (HMXB) system that was discovered with a rocket-borne proportional counter in 1967 (G. Chodil et al. 1967). The compact object in the HMXB was determined to be a neutron star (NS) when periodicity ($P_{\rm spin}$) of ∼4.8 s was detected from the X-ray data (R. Giacconi et al. 1971), making it one of the first detected X-ray pulsars. The system is an eclipsing binary with an almost circular orbit (E. Schreier et al. 1972; H. Raichur & B. Paul 2010; M. Klawin et al. 2023). The companion star, V779 Cen, was identified as an O6-8 III star with a mass of $\sim 21 M_{\odot}$ with a radius of $\sim 12 R_{\odot}$ (J. B. Hutchings et al. 1979). The NS mass was estimated to be $1.34^{+0.16}_{-0.14} M_{\odot}$ from optical spectroscopic data (A. van der Meer et al. 2007). The binary has an orbital period ($P_{\rm orb}$) of about 2.09 days with a period decay rate of ($\dot{P}_{\rm orb}/P_{\rm orb}$) approximately $-1.8 \times 10^{-6}\,{\rm yr}^{-1}$ (H. Raichur & B. Paul 2010; M. Falanga et al. 2015; M. Klawin et al. 2023).

A cyclotron line has been observed in the source spectrum near ∼30 keV, giving a magnetic field strength of about 3×10^{12} Gauss (F. Nagase et al. 1992; G. Tomar et al. 2021). Spin phase–resolved analysis of the same NuSTAR study showed a positive correlation of the cyclotron line energy with source flux (T. Tamba et al. 2023). From the stable pulse profile across the entire observation, the study also concluded the presence of a stable accretion stream in the binary system. Subsequent study of the cyclotron line with NuSTAR over two orbits showed that there was no clear correlation between luminosity of the source and the cyclotron line energy, with a possible critical luminosity lying in the range $0.5–4 \times 10^{37}\,{\rm erg\,s}^{-1}$ (Q. Liu et al. 2024). Polarization measurements from the source with IXPE show no detected polarization in the low-intensity level, while the brighter observation gives a very low degree of polarization of ∼6% (S. S. Tsygankov et al. 2022). The low polarization signal was explained by a combination of multiple factors, including overheated upper atmosphere from the NS and mixing of polarization signals from the two magnetic poles.

Cen X–3 is one of the most studied HMXB systems. The luminosity of Cen X–3 varies by almost a factor of 40, with the maximum luminosity reaching $5 \times 10^{37}\,{\rm erg\,s}^{-1}$, which indicates that the predominant mode of accretion is probably via a disk (H. Raichur & B. Paul 2008; S. Suchy et al. 2008). The orbit-averaged long-term light curve shows strong intensity variations, and a period of 120–165 days was noticed in earlier observations (W. C. Priedhorsky & J. Terrell 1983). A superorbital period of 220 days was proposed with 6 yr of MAXI data, which was attributed to the precession of the accretion disk (Á. Torregrosa et al. 2022). However, subsequent analysis of longer-duration data of Cen X–3 from MAXI has not shown any persistent long-term periodicity (A. Balu et al. 2024). Investigations of the long-term light curves have further revealed that the eclipse ingresses and egresses were shorter and sharper in high-intensity levels compared to low-intensity levels, indicative of varying disk obscuration (H. Raichur & B. Paul 2008; J. Devasia et al. 2010). A tentative link between torque reversal and orbital profile was also suggested from long-term observations (Z. Liao & J. Liu 2024). In a further study of the orbital characteristics with long-term intensity variations with MAXI/Gas Slit Camera (GSC), A. Balu et al. (2024) found an increase in the hardness ratio in the orbital phases between 0.5 and 0.9 in the lowest intensity level, which can be interpreted as due to the presence of a wake-like structure.

An iron emission line was first discovered in the source spectrum from the 8th Orbiting Solar Observatory (OSO−8) observation (N. E. White et al. 1983). The iron line was later found to be a combination of emission lines from multiple

ionization states of iron, namely, neutral and near-neutral iron (henceforth denoted as Fe I), helium-like iron (Fe XXV), and hydrogen-like iron (Fe XXVI) species from ASCA data (K. Ebisawa et al. 1996). The presence of the three iron lines has been used to probe different regions of the reprocessing environment as they originate from different regions in the binary environment (K. Ebisawa et al. 1996; S. Naik & B. Paul 2012).

Even though iron fluorescence emission is ubiquitous in X-ray binaries (A. Giménez-García et al. 2015), pulsations in the iron line have only been observed in a few sources like Cen X–3 (C. S. R. Day et al. 1993; T. Tamba et al. 2023), Her X−1 (C. S. Choi et al. 1994; D. Vasco et al. 2013), V0332+53 (S. D. Bykov et al. 2021), and GX 301−2 (K. Roy et al. 2024). Other emission lines have also been observed to be variable with NS rotation, like the Ne IX Kα fluorescent line in the ultracompact X-ray binary 4U 1626−67 (A. Beri et al. 2018).

Pulse phase–dependent modulation in the iron Kα emission line was discovered in Cen X–3 with GINGA data (C. S. R. Day et al. 1993) and later confirmed with NuSTAR data (T. Tamba et al. 2023). However, for both these cases, the entire iron Kα complex was modeled with a single Gaussian line. Iron line variations with spin of the NS can be produced if there is an anisotropic distribution of matter in the line-producing region and if the light travel time across the region is smaller than the pulse period of the NS. For the case of slow rotating pulsars ($P_{\rm spin} \gtrsim 100$ s) like GX 301−2 or Vela X−1, the light travel distance corresponding to the pulse period of the NS is larger than the binary orbit; therefore, any anisotropies in the wider reprocessing environment can give rise to pulse phase dependency of the iron emission lines. For fast spinning pulsars ($P_{\rm spin} \lesssim 10$ s) like Her X−1, 4U 1626−67, and Cen X–3, the pulse phase dependence of fluorescent lines can only be produced close to the NS. In Cen X–3, the binary orbit size (∼40 lt-s) is much larger than the light travel distance corresponding to the pulse period of the NS (∼4.8 lt-s), making it possible to study the anisotropies in the line-producing region in the inner orbital region in the vicinity of the NS.

The large effective area and good spectral resolution of XMM-Newton allow us to resolve the iron fluorescence emission complex and study the variation in the individual iron lines. We take advantage of the excellent spectral and timing properties of XMM-Newton to investigate the pulse phase dependence of the individual iron emission lines from an archival observation of Cen X–3 taken in 2006. We structure the manuscript as follows: In Section 2, we introduce the details of XMM-Newton instrument, the observation details, and the data reduction techniques. In Section 3, we describe the data analysis methods and the results. In Section 4, we discuss the implications of the results, and we summarize the study in Section 5.

2. Instruments, Observation, and Data Reduction

XMM-Newton (F. Jansen et al. 2001), an X-ray observatory of the European Space Agency, consists of three X-ray detectors named European Photo Imaging Camera (EPIC) at the focal plane of three X-ray telescopes. Two of the EPIC cameras have metal–oxide–semiconductor (MOS)CCD detectors (M. J. L. Turner et al. 2001), and the third contains a PN CCD detector (L. Strüder et al. 2001). There are two additional Reflection Grating Spectrometer telescopes for high-resolution X-ray spectroscopy (J. W. den Herder et al. 2001) and an Optical Monitor for optical and UV imaging (K. O. Mason et al. 2001).

We present the results from analysis of one of the longest observations of Cen X–3 with XMM-Newton taken on 2006 August 12 (MJD 53898.938–MJD 53899.860). The observation (ObsID: 0400550201), lasting ∼81 ks, was taken in the TIMING MODE with the MOS2 and PN detectors. The EPIC cameras operate in the energy range of 0.5–10.0 keV. We have utilized the EPIC−PN data for this work due to its large effective area.

We used the Science Analysis System (SAS) version 19.1.0 for all data extractions. We followed the instructions provided in the SAS Data Analysis Threads.[3] The data reduction procedures relevant for TIMING MODE were followed from the XMM-Newton ABC Guide.[4] We have used the latest calibration files to reduce the data.

We have only considered events with `FLAG = 0` and with `PATTERN <= 4` for the PN data.[5] The source region was extracted from columns centered around the brightest zone of the image (`RAWX IN [28:44]`), and the background was selected from columns away from the source region (`RAWX IN [5:15]`). Solar system barycentre correction was performed on the event file by SAS tool `barycen`. The photon times of arrivals were corrected for the motion of NS in the binary orbit using orbital ephemeris from M. Klawin et al. (2023). The source and background light curves with a resolution of 0.0001 s and spectra were generated from the aforementioned regions. The response and ancillary files were generated using the `rmfgen` and `arfgen` tools. We checked for pileup in the data using the SAS tool `epatplot` and found no noticeable pileup.

The long-term light curve from RXTE/All Sky Monitor (ASM) binned with the orbital period of Cen X–3 is shown in Figure 1. The epoch of the XMM-Newton observation is shown in red in the same.

3. Data Analysis

3.1. Timing Analysis

Cen X–3 is an eclipsing binary source with a high inclination of around 79° (G. Sanjurjo-Ferrín et al. 2021). The orbital X-ray intensity is plotted in Figure 2 from RXTE/ASM in the 2–10 keV energy range using the orbital ephemeris from M. Klawin et al. (2023). The XMM-Newton observation was taken during the out-of-eclipse phase of the orbit between the orbital phase 0.297–0.738, where zero phase is assigned to mideclipse.

The light curve shows variability at multiple timescales along with pulsations at ∼4.8 s. The pulse period of the source was calculated to be 4.805069 (1) s from the barycentre and binary orbit-corrected data using the epoch folding tool `efsearch`. The average pulse profile from the entire observation obtained by folding the light curve is plotted in Figure 3. The pulse profile of Cen X–3 in the 0.5–10 keV energy range is double-humped in nature, with the primary and secondary peak having a phase separation of ∼0.45. The pulse fraction (PF) of the 0.5–10 keV light curve is 51.5% ± 0.2%, where the PF for a pulse profile (P) is defined as $\mathrm{PF} = P_{\rm max} - P_{\rm min})/(P_{\rm max} + P_{\rm min})$.

[3] https://www.cosmos.esa.int/web/xmm-newton/sas-threads
[4] https://heasarc.gsfc.nasa.gov/docs/xmm/abc/abc.html
[5] https://www.cosmos.esa.int/web/xmm-newton/sas-threads

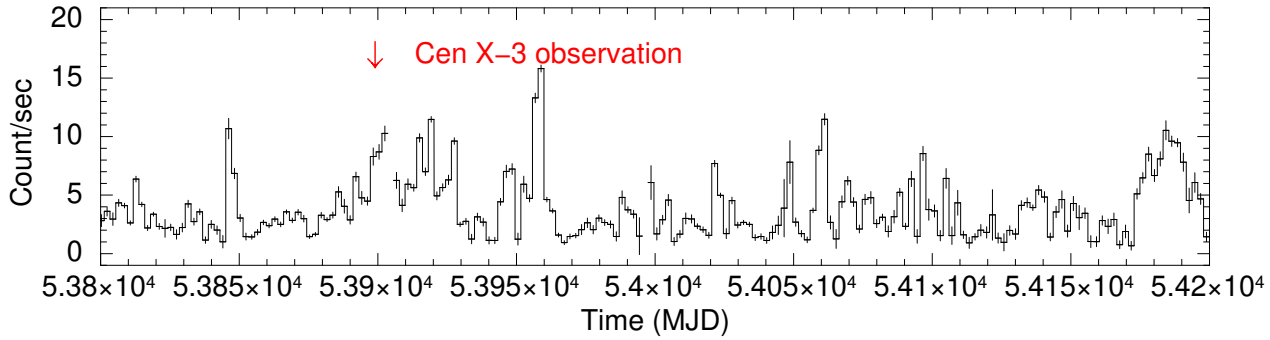

Figure 1. The long-term light curve of Cen X–3 with RXTE/ASM is plotted in black with a bin size corresponding to the orbital period of the source. The red marker corresponds to the XMM-Newton observation of the source.

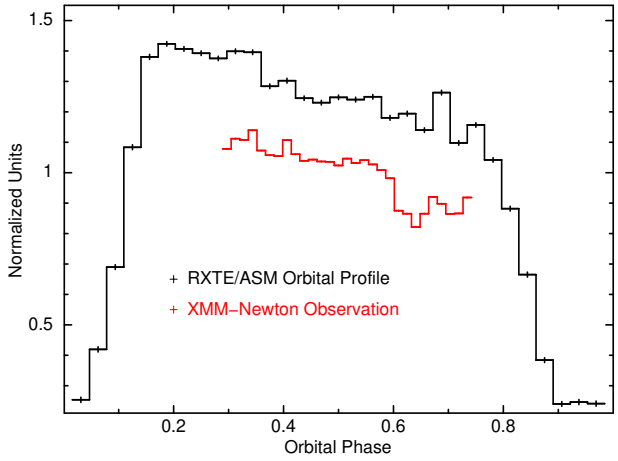

Figure 2. The long-term orbital profile of Cen X–3 is plotted in black from RXTE/ASM in the 2–10 keV energy range normalized by the average count rate. The XMM-Newton observation is plotted in red normalized by the average count rate.

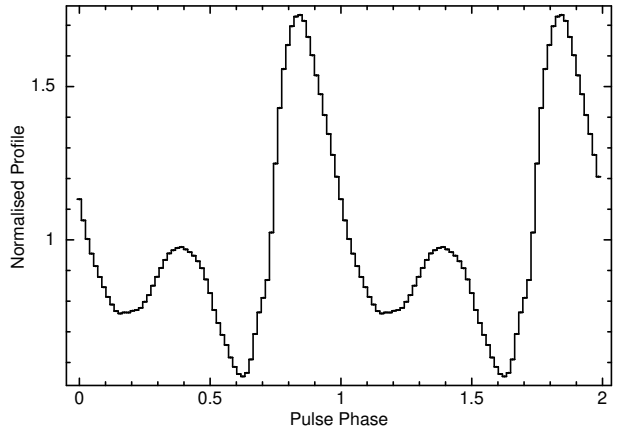

Figure 3. The pulse profile obtained by folding the 0.5–10 keV XMM-Newton EPIC−PN light curve with the pulse period of the pulsar of 4.805069 s normalized by the average count rate of the source.

3.2. Time-averaged Spectroscopy

The spectrum of the source was fitted using the `HEASoft` spectral fitting tool XSPEC version 12.12.0 (K. A. Arnaud 1996). The absorption by interstellar medium was modeled using the Tuebingen–Boulder absorption model `TBabs` with abundance taken from J. Wilms et al. (2000) and the photoelectric cross sections from D. A. Verner et al. (1996). The spectra used in this study have been optimally binned based on J. S. Kaastra & J. A. M. Bleeker (2016). For very bright X-ray sources, the spectra from XMM-Newton EPIC−PN cameras can suffer from pileup effects, but no clear pileup was observed in this source. The PN spectrum in timing mode has some energy calibration uncertainties[6] that are more prominent at lower energies, and since the main purpose of the current study is to investigate the iron line variations, we only consider the spectra in a limited energy band of 5.0–9.0 keV around the iron fluorescent line. We fitted the 5.0–9.0 keV EPIC−PN spectrum of Cen X–3 to study the iron fluorescent emission.

The X-ray continuum was modeled with an absorbed power-law component. Multiple emission lines were present on top of the continuum emission. In total, we detected five emission lines in the aforementioned energy range, the most prominent being the 6.4 keV neutral iron Kα line. The final spectral model used is `tbabs×` (`powerlaw` + 5 ×`Gaussians`). The fluorescence emission from highly ionized Fe XXV and Fe XXVI species was also present, along with iron Kβ and nickel Kα emission lines. The best-fit spectral model and the data are plotted in Figure 4. The emission lines from near-neutral iron Kα (red), iron XXV (blue), iron XXVI (green), iron Kβ (orange), and nickel Kα (cyan) could be resolved from the EPIC−PN spectrum (G. Sanjurjo-Ferrín et al. 2021; Figure 4). The line detection significance quantified as the ratio of the strength of the lines and the error on the estimate of the line strength for the Fe I Kα, Fe XXV Heα, Fe XXVI Lyα, Fe Kβ, and Ni Kα was calculated to be 68σ, 36σ, 15σ, 22σ, and 11σ. The equivalent width of all the emission lines is in the range of 10–50 eV. The best-fit spectral parameters are given in Table 1, with errors quoted at 90% confidence level.

3.3. Pulse Phase–resolved Spectroscopy

We performed pulse phase–resolved spectroscopy of the entire observation to study the variability of the fluorescence lines with the spin of the NS using barycentre and orbital motion corrected event data. The pulse profile was divided into 20 equal phase bins, and the spectrum was extracted from each phase segment. The same spectral model we fitted to the phase-averaged spectrum was used to fit the spectrum from each of these data sets. The centers and widths of the emission lines were fixed to the best-fit values obtained from the phase-averaged spectrum due to limited photon statistics. We put emphasis on the three Kα lines from neutral, helium-like, and hydrogen-like iron species and the iron Kβ line, which are the most prominent.

[6] https://xmmweb.esac.esa.int/docs/documents/CAL-TN-0083.pdf

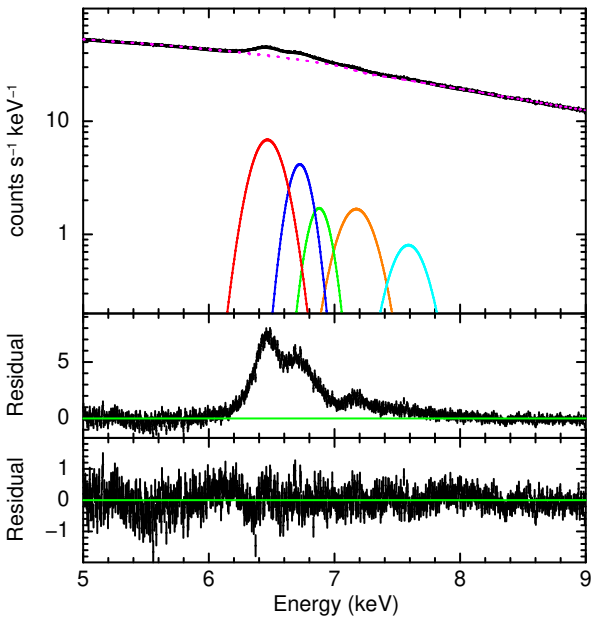

Figure 4. The 5.0–9.0 keV XMM-Newton EPIC−PN spectrum of Cen X–3 is shown in the figure. The top panel contains the data and the best-fit model components. The middle panel shows the residuals when the strength of the emission lines are all set to zero. The bottom panel shows the residuals between the data and the best-fit model.

The emission line strength, i.e., the normalization of the Gaussian profile used to model the emission line, is plotted in Figure 5 as a function of pulse phase. The pulse profile in the 0.5–10 keV range is plotted in black for reference. The Fe I Kα (blue), Fe XXV Heα (orange), Fe XXVI Lyα (red), and Fe Kβ (purple) all show variability with the pulse phase, as seen in Figure 5. The modulation in all four iron line intensities is quite similar, and the peak of the line emission is not aligned with the peak of the pulse profile. We discuss the results further in Section 4.

3.4. Variation of Iron Emission Lines with Different Trial Pulse Periods

In order to confirm the presence of modulations in the iron emission lines with the pulse period of the NS, we performed pulse phase–resolved spectroscopy with multiple trial periods on either side of the NS pulse period of 4.805069 s. A trial period range of ±0.1 s around the pulse period was investigated with a period resolution of 0.002 s, and a range of ±1.0 s was investigated with a period resolution of 0.02 s. For each trial period, we divided the data into 20 equal phase bins and fitted the same spectral model used in the phase-averaged analysis (Section 3.2) to estimate the iron line strength in each phase interval. For each of the four iron line components, the 20 measured line flux values were fitted to a constant, and the chi-square was determined for the best fit. This chi-square acts as a proxy for the strength of modulation present in the line emission for each trial period. The resulting chi-square distributions for near-neutral Fe I Kα, Fe XXV Heα, Fe XXVI Lyα, and Fe Kβ are shown against the trial periods in Figure 6.

The four iron emission lines clearly show a peak in chi-square only at the NS pulse period of 4.805069 s (Figure 6). Therefore, we can establish from this independent analysis that the variation of the iron fluorescent emission lines with

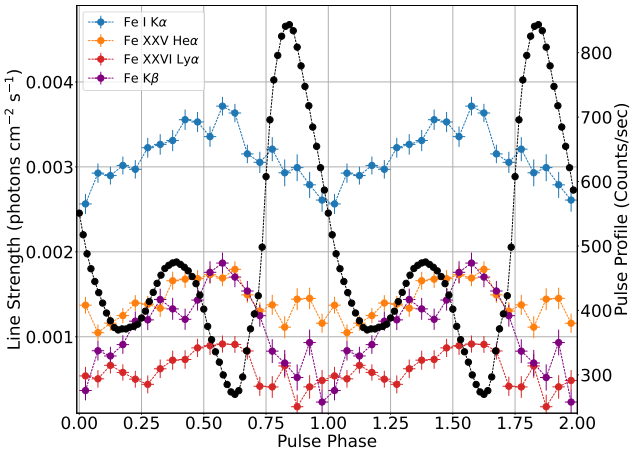

Figure 5. The variation of the four emission lines, from near-neutral Fe Kα (blue), Fe XXV Heα (orange), Fe XXVI Lyα (red), and Fe Kβ (purple) is plotted with the pulse phase of the NS along with the pulse profile in the 0.5–10 keV range (black).

Table 1
Best-fit Spectral Parameter Corresponding to the Phase-averaged Spectrum of Cen X–3 with Errors Quoted at 90% Confidence Interval

Model	Parameter	Units	Best-fit Value
Absorption	$N_{\rm H}$	10^{22}	$8.18^{+0.32}_{-0.32}$
Power-law	Γ	...	$1.27^{+0.01}_{-0.01}$
	Norm[a]	...	$0.60^{+0.01}_{-0.01}$
Fe Kα	Norm[b]	10^{-3}	$2.99^{+0.04}_{-0.04}$
	Eqw	eV	$52.25^{+0.87}_{-0.94}$
Fe XXV	Norm[b]	10^{-3}	$1.36^{+0.04}_{-0.04}$
	Eqw	eV	$23.80^{+0.67}_{-0.67}$
Fe XXVI	Norm[b]	10^{-4}	$5.85^{+0.40}_{-0.40}$
	Eqw	eV	$10.75^{+0.77}_{-0.76}$
Fe Kβ	Norm[b]	10^{-3}	$1.01^{+0.05}_{-0.05}$
	Eqw	eV	$20.22^{+0.87}_{-0.85}$
Ni Kα	Norm[b]	10^{-4}	$5.41^{+0.49}_{-0.49}$
	Eqw	eV	$11.91^{+1.11}_{-1.03}$
Flux[c]	...	10^{-9}	$3.64^{+0.02}_{-0.02}$
χ^2 (d.o.f.)	...	...	1012.12 (791)

Notes.
[a] The power-law normalization is in units of photons keV^{-1} cm $^{-2}$ at 1 keV.
[b] The units of the normalization for the Gaussian profile is the total number of photons s^{-1} cm $^{-2}$ in the line.
[c] The units for flux is erg s^{-1} cm^{-2}.

rotation of the NS found in Section 3.3 is an actual signal with a significant detection.

3.5. Orbital-phase-dependent Pulse Phase–resolved Spectroscopy

Pulsating iron line emission can originate from various parts of the binary environment that are smaller in size than the light

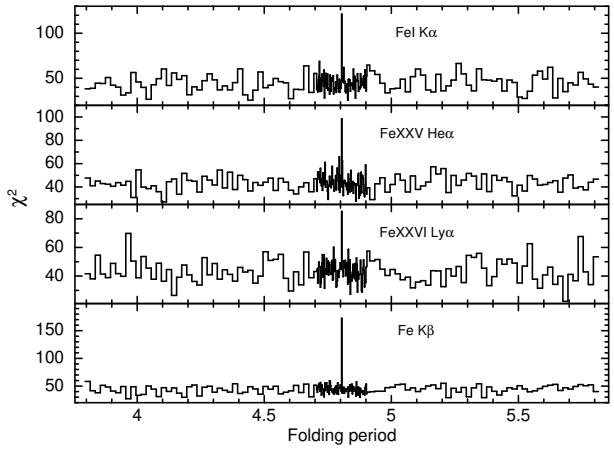

Figure 6. The figure shows the variation of the chi-square value of the pulse phase modulation of the iron line flux for 20 pulse phase bins with different trial pulse periods. The results for Fe I Kα, Fe XXV Heα, Fe XXVI Lyα, and Fe Kβ are plotted from the top in different panels.

travel distance for the pulse period of the NS. Any line-forming region in the binary system whose position with respect to our line of sight to the NS changes with orbital phase is expected to show a variable phase difference between line flux modulation and the total pulse profile in different orbital phases. To evaluate this, we divided the total observation into four orbital phase segments. In each of the four segments, we probed the pulse phase dependence of the iron line emission similar to Section 3.3. The results for near-neutral Fe Kα, Fe XXV Heα, Fe XXVI Lyα, and Fe Kβ are plotted in different panels in Figure 7 in different colors for the different orbital phase segments. The orbital segments span approximately from 0.297 to 0.407, 0.407 to 0.518, 0.518 to 0.628, and 0.628 to 0.738 and are plotted in Figure 7 in black, orange, cyan, and blue, respectively. The near-neutral iron Kα line shows clear pulsations in all the segments. The most interesting observation is that the minima of the near-neutral iron Kα line strength occur at a similar pulse phase for each of the orbital phase segments. A similar pattern is also seen in the iron Kβ emission line. In segments where pulsations have been detected, the modulation of the helium-like and hydrogen-like iron emission shows minima at a similar pulse phase. The strength of the Fe XXV Heα line in the fourth segment was low compared to the other segments, and no pulsations were detected in the Fe XXV Heα line. This is in agreement with time-resolved analysis with the XMM-Newton data (G. Sanjurjo-Ferrín et al. 2021). Pulse phase modulation was not clearly detected in the second segment for the Fe XXVI Lyα line.

4. Discussion

In this manuscript, we report the results from the analysis of data from an XMM-Newton observation of Cen X–3 taken in the out-of-eclipse part of its binary orbit. Cen X–3 was observed for ∼81 ks between the orbital phase of ∼0.297–0.738. Pulsations were detected in the source with a period of 4.805069 s. The 5.0–9.0 keV spectrum was modeled with an absorbed power-law continuum with multiple emission lines from iron and nickel Kα line. The detection significance of the Fe I Kα, Fe XXV Heα, Fe XXVI Lyα Fe Kβ, and Ni Kα was calculated to be 68σ, 36σ, 15σ, 22σ, and 11σ, respectively.

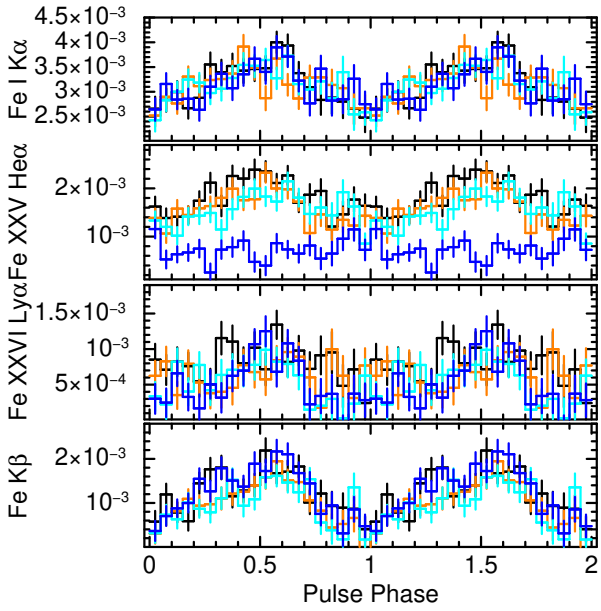

Figure 7. The figure shows the variation of the pulse phase modulation of the iron line fluxes as a function of orbital phase. From the top, the results for Fe I Kα, Fe XXV Heα, Fe XXVI Lyα, and Fe Kβ are plotted in different panels. The results from four different orbital phase segments are plotted in black (0.297–0.407), orange (0.407–0.518), cyan (0.518–0.628), and blue (0.628–0.738) colors.

Long-term data from RXTE/ASM show wide variations in the intensity of Cen X–3. Similar studies performed with MAXI/GSC showed that Cen X–3 exhibits multiple luminosity levels with no apparent superorbital period (A. Balu et al. 2024). From the long-term RXTE/ASM light curve, we can see that during this observation, the source was in a high-intensity level (Figure 1). X-ray luminosity states in Cen X–3 have been studied in the past, and several hypotheses have been put forward to explain the multiple source intensities. The source was captured in a transition from low-intensity to high-intensity level with the Chandra telescope (G. Sanjurjo-Ferrín et al. 2024). The transition was hypothesized to be due to the cooling of a large chunk of matter, which increased the mass accretion onto the NS (G. Sanjurjo-Ferrín et al. 2024). From RXTE observations of Cen X–3, it was proposed that an aperiodically precessing warped accretion disk is probably responsible for the changes in intensity states of Cen X–3 (H. Raichur & B. Paul 2008). However, a later study of Cen X–3 with AstroSat showed that spectral shape and pulse profile are different in different luminosity states, pointing to accretion column origin (R. Bachhar et al. 2022).

Emissions from different ionization states of iron probe different regions around the NS. Intensity and equivalent width variations of the three iron K lines with orbital phase of Cen X–3 were investigated with a Suzaku observation (S. Naik et al. 2011). Using ASCA (K. Ebisawa et al. 1996) and XMM-Newton (S. Naik & B. Paul 2012) observations, it was shown that the 6.4 keV fluorescence lines may originate from close to the NS, while the lines at 6.7 and 6.97 keV are produced further away, either in the photoionized wind of the MS star or in the accretion disk corona. The high resolving power of XRISM allows investigation of the Doppler motion of the 6.4 keV iron Kα emission line. From the measurements of radial velocity around the binary orbit, the source of the fluorescent line could not be attributed to either the NS surface,

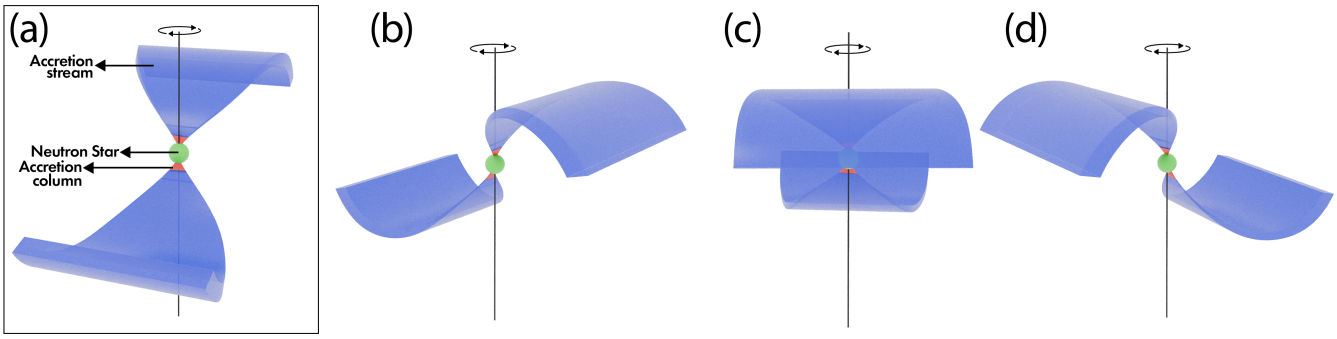

Figure 8. The figure shows a schematic representation of Cen X–3. The compact object (green), accretion column (red), and the accretion stream (blue) are shown in different colors in panel (a). In panel (b)–(d), we see a different line of sight to the NS. Panel (c) shows when the accretion stream intercepts our line of sight to the NS.

the companion stellar wind, the companion star surface, or the accretion wake alone (Y. Mochizuki et al. 2024). Elaborate models of iron fluorescence are required for the complete understanding of the origin of the emission line.

In this work, we confirmed the pulse phase variation of the three iron Kα lines and report the pulse phase variation observed in the iron Kβ line. We investigated the reprocessing region in Cen X–3 using the pulse phase dependency of the iron emission lines. The variations of the four emission lines with pulse phase are plotted in Figure 5. All four lines show significant variability with the pulse phase of the NS. The pulse phase variability of the Fe I Kα, Fe XXV Heα, Fe XXVI Lyα, and Fe Kβ lines were detected at 8.8σ, 8.2σ, 5.5σ, and 18.9σ. The modulations of the four iron lines are single-peaked in nature, unlike the pulse profile, which has two peaks. The pulse phase variability of the iron fluorescent lines could be well fitted with a sinusoidal function on top of a constant value. The modulation in the iron line with pulse phase was quantified by taking the ratio of the sine amplitude to the constant fit. The modulation factor of the Fe XXVI Lyα ($31.0\% \pm 7.8\%$) is much stronger than the Fe XXV Heα ($18.1\% \pm 3.0\%$) and the near-neutral iron Kα ($13.1\% \pm 1.6\%$) emission line. The modulation factor of the Kβ line was calculated to be $50.5\% \pm 5.6\%$. The pulse phase corresponding to the minima of pulse phase dependence for the four emission lines coincides (Section 3.3), indicating a common origin.

The evolution of the line intensity during eclipse egress in Cen X–3 shows that the highly ionized line species has a smaller "rise time," and hence it originates closer to the NS (K. Ebisawa et al. 1996; S. Naik & B. Paul 2012), while the neutral iron Kα emission line takes about 40 ks to reach its maximum value as Cen X–3 comes out of eclipse (S. Naik & B. Paul 2012). The neutral line-forming region probably encompasses a region close to 55 lt-s in size. A similar calculation of the line-forming region with ASCA data showed a size of $\sim$28 lt-s (K. Ebisawa et al. 1996). This region is probably responsible for the nonpulsating component. However, the region emitting the pulsed component of the iron line should be much more compact and within 4.8 lt-s as the pulse period of the NS is only about 4.8 s. The pulse phase–dependent modulation in the four iron emission lines indicates the existence of a reprocessing region close to the NS.

Naively, an anisotropic distribution of matter producing the pulse phase variability can be from clumps in the stellar wind, which is expected from the massive O-type companion star in Cen X–3. However, the identical pulse phase modulation of the four iron fluorescent lines across a wide orbital phase range (Section 3.5) shows no significant change, indicating that the reprocessing emission must come from structures that are much more persistent than clumpy wind material. The absence of any change of the relative phase between modulation of the iron lines and the pulse profile with the orbital phase of Cen X–3 indicates that the component responsible for the pulsed emission must have very little relative motion with respect to the NS and the observer. The absorption column density and the strength of the iron line show similar variations with pulse phase (C. S. R. Day et al. 1993). The absorption column density as well as the emission line strength in Cen X–3 is maximum between the two peaks in the pulse profile of Cen X–3 (C. S. R. Day et al. 1993).

In the case accretion by Roche Lobe overflow happens in Cen X–3, then the location where accreted matter from the secondary star meets the accretion disk in Cen X–3 can be the origin of the pulsed component of the iron emission lines. In this scenario, the pulse phase modulations from the multiple iron emission lines are expected to be in phase. The location of the hot spot, however, is expected to vary with respect to our line of sight to the NS in different orbital phases. The companion star surface sustains a large solid angle with respect to the NS, and therefore, it is not expected to produce a very sharp pulse phase modulation in the emission component. Another possible origin of the anisotropy can be from the wake-like structure observed in Cen X–3 (A. Balu et al. 2024); however, this structure is also expected to show orbital variation in the pulse phase modulations of the multiple iron lines. In the current observation, we see that the iron lines do not show significant variability with phase, rejecting this scenario as the origin of the pulsed emission lines.

We propose a possible physical configuration to explain the observed pulse phase variation of iron fluorescence lines in Cen X–3. A sketch of the NS system is given in Figure 8(a), similar to Figure 10 of S. S. Tsygankov et al. (2022). The NS is shown in green, the accretion column in red, and the accretion stream channeling matter from the accretion disk to the NS is shown in blue. The accretion stream corotates with the NS spin motion as it is attached to the magnetic field of the compact object. X-rays from the NS are emitted from the accretion column at the base of the accretion stream. Assuming the accretion column forms a broad beam, the accretion stream partially obstructs the view of the X-ray from the accretion column as the base of the accretion stream, where the accretion stream meets the accretion disk, comes into our line of sight (Figures 8 (b)–(d)). The presence of the accretion stream produces two humps in the pulse profile with an increase of absorption column density in between the two peaks. For the same orientation of the NS, the base of the

accretion stream (Figure 8 (c)), would also produce an increase in fluorescent emission. Such an increase in absorption column density and iron line strength between the two peaks of the pulse profile has been observed in Cen X–3 with GINGA data (C. S. R. Day et al. 1993). We see a similar pattern in the pulse phase dependence of the four iron fluorescence strength and pulse profile (Figure 5) consistent with GINGA results. At any orbital phase, the pulse phase variations of the iron lines are expected to have the same phase relation with the pulse profile, i.e., the maximum intensity of the lines occurring at the dip between the two pulse peaks. The similarity of the shape of the pulse variation of the four iron line (Section 3.3) and their persistence with orbital motion (Section 3.5) of Cen X–3 can be reasonably explained by the above scenario. Therefore, the accretion stream cutting the line of sight to Cen X–3 can produce the observed pulse phase dependence of the multiple iron lines.

5. Summary

In this work, we analyze an XMM-Newton observation of Cen X–3 to study the binary reprocessing environment. Multiple prominent lines were present in the source spectrum, and we have carried out pulse phase–resolved spectroscopy to investigate the three Kα lines from near-neutral, helium-like, and hydrogen-like iron and the iron Kβ emission lines. The results from the phase–resolved analysis can be summarized as follows:

1. The near-neutral Fe I Kα, Fe XXV Heα, Fe XXVI Lyα, and Fe Kβ lines are variable with the pulse phase of the NS.
2. The Fe XXVI Lyα (31%) and Fe Kβ (51%) showed much stronger modulation than the Fe XXV Heα (18%) and the Fe I Kα (13%) emission line.
3. The pulsating and nonpulsating iron fluorescent emission probably originate from different locations in the binary system.
4. The shape of the pulse phase modulations appears in phase and does not show significant variation with the orbital motion of the NS.
5. The pulsating component for the four iron fluorescent lines probably shares a common origin and must originate within the light travel distance corresponding to the pulse period of the NS.
6. The pulsating component can originate from an accretion stream intersecting the line of sight to the accretion column of the NS from the observer.

Acknowledgments

We thank the referee for the useful comments and suggestions that improved the quality of this paper. K.R. would like to thank Gulab Dewangan and Matteo Guainazzi for the discussion regarding instrumental effects in EPIC−PN spectrum. K.R. would like to thank Arunima for creating the illustrations.

ORCID iDs

Kinjal Roy https://orcid.org/0000-0002-7391-5776
Hemanth Manikantan https://orcid.org/0000-0001-9404-1601
Biswajit Paul https://orcid.org/0000-0002-8775-5945

References

Arnaud, K. A. 1996, in ASP Conf. Ser. 101, Astronomical Data Analysis Software and Systems V, ed. G. H. Jacoby & J. Barnes (San Francisco, CA: ASP), 17
Bachhar, R., Raman, G., Bhalerao, V., & Bhattacharya, D. 2022, MNRAS, 517, 4138
Balu, A., Roy, K., Manikantan, H., Tamang, A., & Paul, B. 2024, A&A, 692, A47
Beri, A., Paul, B., & Dewangan, G. C. 2018, MNRAS, 475, 999
Bykov, S. D., Filippova, E. V., Gilfanov, M. R., et al. 2021, MNRAS, 506, 2156
Chodil, G., Mark, H., Rodrigues, R., et al. 1967, PhRvL, 19, 681
Choi, C. S., Nagase, F., Makino, F., et al. 1994, ApJ, 437, 449
Day, C. S. R., Nagase, F., Asai, K., & Takeshima, T. 1993, ApJ, 408, 656
den Herder, J. W., Brinkman, A. C., Kahn, S. M., et al. 2001, A&A, 365, L7
Devasia, J., Paul, B., James, M., & Indulekha, K. 2010, RAA, 10, 1127
Ebisawa, K., Day, C. S. R., Kallman, T. R., et al. 1996, PASJ, 48, 425
Falanga, M., Bozzo, E., Lutovinov, A., et al. 2015, A&A, 577, A130
Giacconi, R., Gursky, H., Kellogg, E., Schreier, E., & Tananbaum, H. 1971, ApJL, 167, L67
Giménez-García, A., Torrejón, J. M., Eikmann, W., et al. 2015, A&A, 576, A108
Hutchings, J. B., Cowley, A. P., Crampton, D., van Paradijs, J., & White, N. E. 1979, ApJ, 229, 1079
Jansen, F., Lumb, D., Altieri, B., et al. 2001, A&A, 365, L1
Kaastra, J. S., & Bleeker, J. A. M. 2016, A&A, 587, A151
Klawin, M., Doroshenko, V., Santangelo, A., et al. 2023, A&A, 675, A135
Liao, Z., & Liu, J. 2024, MNRAS, 529, L130
Liu, Q., Wang, W., Santangelo, A., et al. 2024, A&A, 687, A210
Mason, K. O., Breeveld, A., Much, R., et al. 2001, A&A, 365, L36
Mochizuki, Y., Tsujimoto, M., Kelley, R. L., et al. 2024, ApJL, 977, L21
Nagase, F., Corbet, R. H. D., Day, C. S. R., et al. 1992, ApJ, 396, 147
Naik, S., & Paul, B. 2012, BASI, 40, 503
Naik, S., Paul, B., & Ali, Z. 2011, ApJ, 737, 79
Priedhorsky, W. C., & Terrell, J. 1983, ApJ, 273, 709
Raichur, H., & Paul, B. 2008, MNRAS, 387, 439
Raichur, H., & Paul, B. 2010, MNRAS, 401, 1532
Roy, K., Manikantan, H., & Paul, B. 2024, MNRAS, 527, 2652
Sanjurjo-Ferrín, G., Torrejón, J. M., Oskinova, L., et al. 2024, A&A, 690, A360
Sanjurjo-Ferrín, G., Torrejón, J. M., Postnov, K., et al. 2021, MNRAS, 501, 5892
Schreier, E., Levinson, R., Gursky, H., et al. 1972, ApJL, 172, L79
Strüder, L., Briel, U., Dennerl, K., et al. 2001, A&A, 365, L18
Suchy, S., Pottschmidt, K., Wilms, J., et al. 2008, ApJ, 675, 1487
Tamba, T., Odaka, H., Tanimoto, A., et al. 2023, ApJ, 944, 9
Tomar, G., Pradhan, P., & Paul, B. 2021, MNRAS, 500, 3454
Torregrosa, Á., Rodes-Roca, J. J., Torrejón, J. M., Sanjurjo-Ferrìn, G., & Bernabéu, G. 2022, RMxAA, 58, 355
Tsygankov, S. S., Doroshenko, V., Poutanen, J., et al. 2022, ApJL, 941, L14
Turner, M. J. L., Abbey, A., Arnaud, M., et al. 2001, A&A, 365, L27
van der Meer, A., Kaper, L., van Kerkwijk, M. H., Heemskerk, M. H. M., & van den Heuvel, E. P. J. 2007, A&A, 473, 523
Vasco, D., Staubert, R., Klochkov, D., et al. 2013, A&A, 550, A111
Verner, D. A., Ferland, G. J., Korista, K. T., & Yakovlev, D. G. 1996, ApJ, 465, 487
White, N. E., Swank, J. H., & Holt, S. S. 1983, ApJ, 270, 711
Wilms, J., Allen, A., & McCray, R. 2000, ApJ, 542, 914